# Effect of various temperatures and strain-rates combinations on the thermomechanical behavior of 42CrMo steel

## A. ABDUL-LATIF[1,2)], F. ABED[3)], CH. OUCIF[4)], G. Z. VOYIADJIS[5)]

[1)] *Laboratoire Quartz, Supméca, 3, rue Fernand Hainaut, 93407 St Ouen Cedex, France*

[2)] *Université Paris 8, IUT de Tremblay, 93290 Tremblay-en-France, France*

[3)] *Department of Civil Engineering, American University of Sharjah, Sharjah 26666, UAE*

[4)] *Institute of Structural Mechanics, Bauhaus-Universität Weimar, Marienstraße 15, D-99423 Weimar, Germany*

[5)] *Department of Civil and Environmental Engineering, Louisiana State University, Baton Rouge, LA, 70803, USA, e-mail: voyiadjis@eng.lsu.edu (corresponding author)*

THIS PAPER INVESTIGATES EXPERIMENTALLY THE THERMOMECHANICAL RESPONSE of 42CrMo steel under several combinations of temperatures and strain-rate. To characterize the flow stress of this highstrength 42CrMo steel, two distinct test configurations were utilized. The first consisted of conventional uniaxial tensile tests conducted at room and elevated temperatures of 523°K, 723°K and 923°K and three quasi-static strain-rates at $0.0015\,\mathrm{s}^{-1}$, $0.015\,\mathrm{s}^{-1}$, and $0.15\,\mathrm{s}^{-1}$. The second test configuration was carried out under dynamic compression using a drop mass bench at room temperature with three different dynamic strain-rates of $300\,\mathrm{s}^{-1}$, $400\,\mathrm{s}^{-1}$, and $500\,\mathrm{s}^{-1}$. Particular attention was paid to key features such as work-hardening (WH), grain size, dynamic strain aging (DSA), formation of microcavities, and their coupling with the influence of temperature/strain-rate combination. The dependence of 42CrMo steels' flow stress on the quasi-static strain-rate at room temperature was almost insignificant. However, the strain-rate sensitivity increased with increasing temperatures. At high temperatures, different factors contributed to modifying the alloy microstructure which has a significant impact on the alloy's mechanical properties. Quantification of the micro-cracks density and fractured specimens' voids was established using scanning electron microscopy (SEM) images. The Voyiadjis–Abed (VA) constitutive model was utilized in describing the flow stress of 42CrMo steels and implemented in the ABAQUS software to develop a robust finite element model capable of accurately simulating variant structural responses of 42CrMo steel alloy.

**Key words:** 42CrMo steel, temperature, strain-rate, mechanical characterization, constitutive modeling.

## 1. Introduction

DUE TO VARIOUS INDUSTRIAL APPLICATIONS, steels have extensively been studied to determine their properties when exposed to various temperature and load-

ing conditions. Their behavior has been analyzed in many research studies. Particular attention has been directed towards investigating the effect of different temperatures and strain-rates on steels' strength and damage behavior. In [1], the authors studied the microstructures of the 304 LN austenitic stainless steel (ASS) at varying engineering strains and strain-rates using electron backscatter diffraction. Further investigation on the thermo-viscoplastic behavior of a 304 austenitic stainless steel was shown in [2] where it was revealed that the strain hardening rate of 304 ASS is strongly affected by the strain-induced martensitic transformation effect. Gordon *et al.* [1] studied the porosity, strain localization, deformation-induced phase transformation, and microstructural response of a metastable austenitic stainless steel under a fatigue regime. The results showed an exceptional fatigue life of metastable 304L produced by directed energy deposition compared to wrought AISI 304L in the as-built condition. The compressive flow stresses of a Selective Laser Melt 316L (SLM-316L) alloy and a commercial 316L (C-316L) allowed under varying strain-rates were investigated in [4]. The authors in [5] investigated the influence of thermal aging on the life cycle of 316 LN austenitic stainless steel under thermomechanical fatigue. The results revealed that the hardening regime is lesser after thermal aging compared to the as-welded condition of the 316 LN austenitic stainless. Abed *et al.* [6] investigated the mechanical response of EN08 steel at quasi-static and dynamic strain-rates and varying temperatures. Less rate-dependency of the strain hardening at room temperature was found, compared to the condition at high temperature. The same authors [7] studied the thermomechanical behavior of C45 steel at varying temperatures for strain-rates up to $0.15\,\mathrm{s}^{-1}$. The results showed a degradation trend of the thermal stresses and an increase in the rate-dependency behavior with temperature increase.

Several investigations have been carried out on the damage behavior of steels. Abed *et al.* [8] evaluated the damage initiation and evolution of steel rebars at low and intermediate loading rates. The results showed that the increase in plastic strain and strain-rates leads to the intensification of the cracks and voids. In [9] the authors studied the behavior of two aluminum alloys in high deformation regime. The results revealed higher strain-rate dependence of AA1050 compared to AA7075. Moreover, several micro- and macro-mechanical and damage modeling approaches have been utilized to describe the flow stress for both low and high-strength steel and alloys [10–16].

The literature exhibits a variety of relevant results derived from significant experiments. Particular attention has been given to the steel 42CrMo (AISI 4140) as a representative low-alloy and medium-carbon steel of high strength. This high-strength alloy is copiously employed in many general-purpose parts including gears, shafts, crowbars, rams, spindles, etc. The chromium and molybdenum in the 42CrMO steel act as alloying elements and enhance the steel's mechanical

properties [17]. It conventionally receives quenching followed by tempering. The latter increases the ductility and toughness but with a reduction in the yield and ultimate strengths. Its effect is to form a strong carbide element that is more complex in nature than the weak carbide formers. Therefore, the steel hardness increases. It was revealed in [18] that, compared to the conventional heat treatment, nucleation of high density and finely dispersed Fe-Cr rich carbides results from the temper bead welding in Grade 22 steel. Moreover, molybdenum, like chromium, forms a strong carbide element producing higher hardness than ordinary steel when the alloy is tempered at higher temperatures. At high temperatures, the carbide phase partitions out, keeping the carbide particles numerous and small [18]. This allows the steel to be used in many industries such as oil and gas and military vehicles [19].

Studies investigating the impact of temperature and strain-rate on 42CrMo have recently been conducted showing their impact on its mechanical behavior [20]. When elevated temperatures are applied, residual stresses and cracks appear on the surfaces, causing rapid tool failure to occur in machining [21]. This, in turn, causes dimensional failure. Additionally, 42CrMo is also prone to undergoing surface failure during welding, as the welded area has a higher probability of degrading and creating intermetallic compounds in comparison to its parent metals [22]. Moreover, when 42CrMo is suitably heat treated, the corrosion resistance of the coated structures such as manganese-phosphate-coated substrates improves [23]. Further studies illustrated that its tensile strength and hardening abilities are enhanced by quenching time and varying temperatures [24].

Tensile and torsion tests have been carried out under varying temperatures on the SCM414 low-alloy steel [25]. It was revealed that the strain-hardening rates are lower with a higher degree of shear deformation via torsion which was due to the combination of high dislocation density and grain refinement. Increasing the strain-rate also affects the temperature rising during deformation as well as the fracture caused by plastic strain localization [26].

Few attempts were made to develop constitutive equations to predict the flow stress of this high-strength alloy over an extensive scope of temperatures and strain-rates [27]. Constitutive models that capture sufficient details without being excessively rigorous are widely preferred in computational applications. Advanced constitutive models attempt to cover a broader range of parameters like microstructural features (dislocations evolutions and their interactions, grain size, etc.) and boundary characteristics. However, increasing the present phenomena in the model increases the number of material constants necessary for the identification of the model, which in turn may limit the practical applications of the model. Thus, an optimal model should maximize the number of deformation phenomena described and simultaneously minimize the number of material constants. Consequently, experiments are required to define them.

Understanding the behavior of alloys at different temperatures and strain rates is necessary for metal forming and cutting processes due to their roles in the local and overall responses [28, 29]. The results showed a cyclic behavior of the true stress with increasing strain at each temperature [28]. In addition, it was shown in [29] that localization of flow and microstructural changes occur at a lower temperature due to forging. It has been shown during machining, for example, that the strain can attain values close to 5 [30]. Also, the temperature in the steel cutting zone increases up to 800°C as shown in [31]. Hence, the viscoplastic response of any metal is always controlled by local mechanisms such as grain size and recrystallization mode during deformation. To predict these processes using numerical tools like finite elements, it is important first to study the behavior of a given alloy at different temperatures and strain-rates combinations. Coefficients of the constitutive equations should then be identified, followed by finite element predictions for a certain process. This methodology was therefore adopted in this work. The thermomechanical response of steel was investigated at different quasi-static tensile strain-rates over a wide range of temperatures. Also, several dynamic compression tests were performed on cylindrical specimens at room temperature using a drop mass bench. Particular attention was given to key features related to viscoplasticity, yielding, strain hardening thermally activated softening [controlled by dynamic recrystallization (DRX) and dynamic recovery (DRV)] and the damage behavior of this alloy. Experimental results were utilized to understand its flow stress and to define the material parameters of the constitutive equations. Lastly, a finite element model capable of simulating various loading scenarios was developed for large-scale problems.

## 2. Characterization methodology

The experimental program performed in this work provides important information about thermomechanical responses of 42CrMo steel at various temperatures and strain-rates combinations. Several mechanical tests, that are important for meeting the requirements for high strength steel characterization, were conducted under different loading conditions. The temperatures used in this work were chosen based on some published results [32, 33]. Most of them dealt with high temperatures. Three elevated temperatures of 250°C (523°K), 450°C (723°K), and 650°C (923°K) as well as room temperature, were considered to provide new additional and complementary results. Besides, temperatures generated during metal cutting are part of this range. Consequently, testing the 42CrMo steel under such specific conditions (temperatures and strain-rates) gives other useful information for many industrial applications.

In general, 42CrMo steel exhibits relatively acceptable ductility and toughness capacity ranges. The chemical analysis of the alloy was performed using wet

methods to determine the average chemical compositions; a summary of these results, in percentage units, is presented in Table 1. Additionally, local analysis was conducted on the 42CrMo alloy, and the initial microstructure observed demonstrates the presence of two phases: ferrite and bainite (Fig. 1).

Table 1. Average chemical compositions of 42CrMo steel alloy.

| Material | C | Cr | Mn | Si | Mo | Fe |
|---|---|---|---|---|---|---|
| 42CrMo | 0.39 | 0.93 | 0.85 | 0.17 | 0.16 | balance |
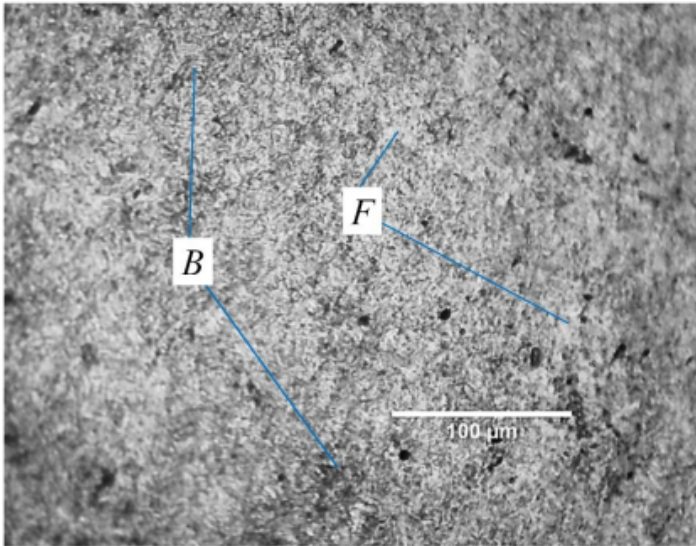


Fig. 1. Optical microscope image for 42CrMo alloy's microstructure.

## 2.1. Specimen material

In this study, more than 20 tensile samples with a length of 70 mm and a diameter of 12 mm were prepared and exposed to different temperatures and quasi-static strain-rates. Figure 2 presents the specimens' dimensions. Note that through the tensile tests at different temperatures, the mechanical properties of 42CrMo steel conducted were presented as engineering stress-strain curves. The main advantage of tensile testing at elevated temperatures is that the stress-strain response simulates the conditions under which damage mechanics occur in several metalworking processes.

For the dynamic tests, the test apparatus consisted of a dynamic-drop mass bench that strikes samples with falling mass at a specified strain-rate. The cylin-
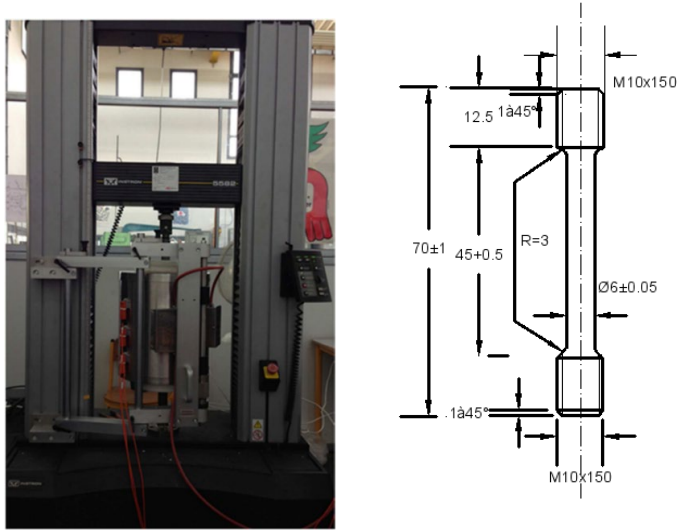
Fig. 2. Dimensions of the high-temperature coupon specimens (in mm) and Zwick/Roell 3-zone high-temperature furnace mounted on the testing machine.
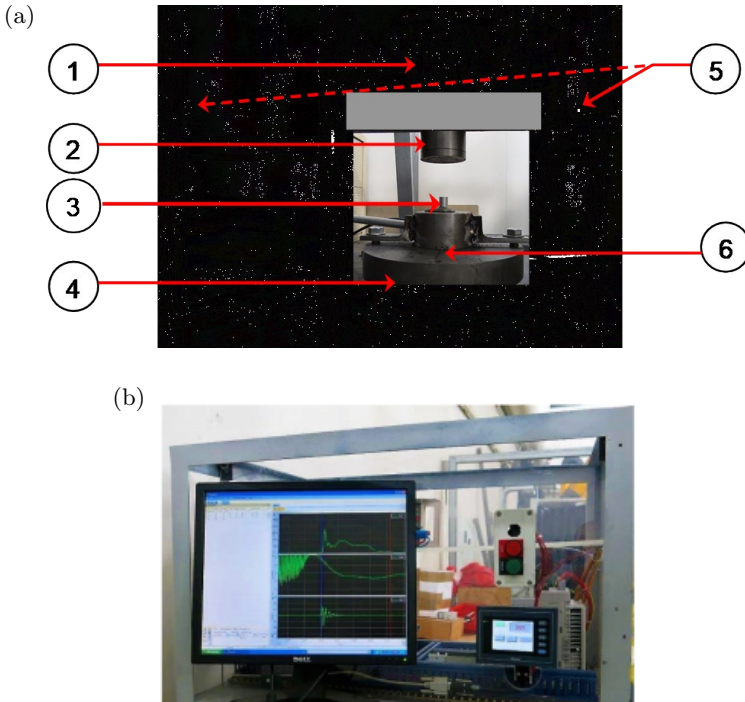


Fig. 3. Instruments used for measuring drop mass bench (a) components: 1 – drop mass, 2 – striker, 3 – sample, 4 – dynamic load cell, 5 – photocells, 6 – displacement transducer; (b) monitoring unit.

drical specimens had a height of 12 mm and a diameter of 6 mm, as shown in Fig. 3. Hammer masses that weighed 17 kg, 22 kg, and 36.4 kg were used to test the specimens and were released from elevations of 4 m, 3 m, and 2 m, respectively. All tests were performed at room temperature. The mean axial strain-rate was determined by $\dot{\varepsilon} = \varepsilon/\Delta t$, where $\varepsilon$ and $\Delta t$ are the total strain and test period, respectively. These assigned parameters correspond to mean strain rates of $500\,\mathrm{s}^{-1}$, $400\,\mathrm{s}^{-1}$, and $300\,\mathrm{s}^{-1}$, respectively. This was done to guarantee that the three strain-rates had approximately equal energy levels, i.e. guaranteeing the iso-energy concept. The true stress-true strain performance of the steel was observed through the displacement and force values that the machine recorded. Other tests were performed if deemed essential.

### 2.2. Quasi-static and dynamic tests

A universal testing machine (UTM) (Instron type 5582) was used to conduct the quasi-static uniaxial tensile tests. The strain-rates applied at varying temperatures were 0.0015, 0.015, and $0.15\,\mathrm{s}^{-1}$, corresponding to 5, 50, and 500 mm/min cross-head speeds, respectively. Several plots of engineering stress-strain curves were presented. Figure 4 illustrates the 42CrMo quasi-static responses at room temperature. The recorded results are not affected by the strain-rates. That is, the response of the alloy does not significantly vary with the differences in these quasi-static strain-rates.
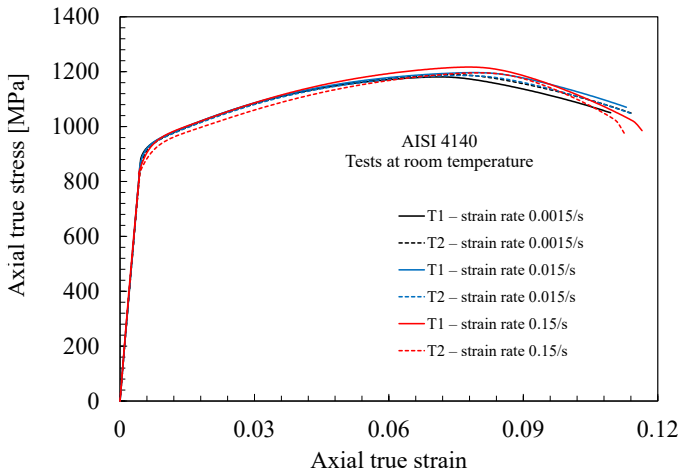


Fig. 4. Stress-strain curves at room temperature and different quasi-static strain-rates.

To evaluate the specimens' behavior at higher temperatures, an independently controlled Zwick/Roell 3-zone high-temperature furnace was placed around the UTM (Fig. 3). The behavior of the material was studied at 523°K,

723°K, and 923°K temperatures and $0.0015\,\mathrm{s}^{-1}$ and $0.15\,\mathrm{s}^{-1}$ strain-rates. A furnace controller (model ME44-180) was used to maintain the specified temperatures over the gage length of the specimen within a $\pm 1$°C range. Each zone was fitted with one thermocouple (Ni/CrNi) while the top, middle, and bottom sections of the specime's gage length were directly fitted with three thermocouples. Each specimen and load train were covered with plates on both the upper and lower ends to conduct the tests. The load was applied when the thermocouples installed on the specimen specified the required temperature with a difference no greater than $\pm 3$°C.

Under dynamic configuration, a dynamic drop mass bench with a $2.5\,\mathrm{kJ}$ maximum kinetic energy and a $10\,\mathrm{m/s}$ maximum impact velocity was utilized to experiment. Equipped to the machine is an accelerometer of $5000\,\mathrm{g}$, a laser beam displacement transducer (series M5L of international Bullier) with a $100\,\mathrm{mm}$ measuring bracket, and a 20-ton dynamic load cell. All these machines were linked to a rapid acquisition chain of $2.5\,\mathrm{MHz}$ to guarantee that the force, acceleration, and displacement are concurrently recorded. The true strain ($\varepsilon_{tr}$) and true stress ($\sigma_{tr}$) were calculated from the engineering values ($\varepsilon_{eng}$ and $\sigma_{eng}$) as $\varepsilon_{tr} = \ln(1 + \varepsilon_{eng})$ and $\sigma_{tr} = \sigma_{eng}(1 + \varepsilon_{eng})$, respectively [13]. Two photocells, shown in Fig. 3, were also used for the same purpose. The photocells' installation and position are essential and are dependent on the location of the striker before impact.

### 2.3. Temperature and strain-rate effects

The stress-strain results of 42CrMo at the four specified temperatures and 0.0015 and $0.15\,\mathrm{s}^{-1}$ quasi-static strain-rates are shown in Figs. 5 and 6, respectively. General, and typical, patterns in the behavior of the material can be captured. These curves illustrate that, at a given strain-rate, higher strength (i.e. ultimate and yield tensile strength) is observed at lower temperatures. At the lower temperatures of 298 and 523°K, the alloy displayed plastic behavior with a significant strain hardening evolution, i.e., behavior showing only phase (i) and phase (ii). In contrast, at the higher temperatures of 723 and 923°K, the alloy displayed stress softening immediately after yielding (Fig. 5). In other words, they demonstrate the four phases, especially at the highest temperature. Actually, at 923°K specifically, the material shows a short work-hardening period effect before displaying viscoplastic behavior accompanied by a negative hardening up to failure. When the strain-rate is $0.15\,\mathrm{s}^{-1}$ (Fig. 6), the most significant difference in the alloy's behavior compared to the aforementioned case is that at 723°K. The stress-strain curve at 523°K and $0.15\,\mathrm{s}^{-1}$ shows that the flow stress experiences a pronounced degradation starting at the 0.05 strain; whereas a further slight increase at 723°K is observed with a crossing occurring at a strain
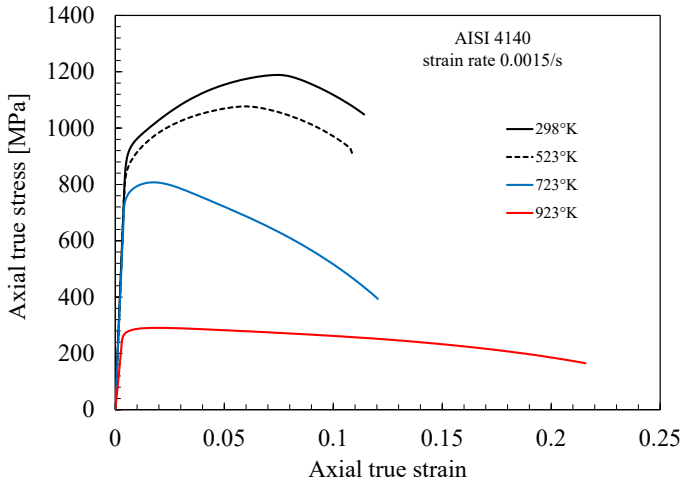
FIG. 5. Stress-strain curves at room temperature and different quasi-static strain-rates.
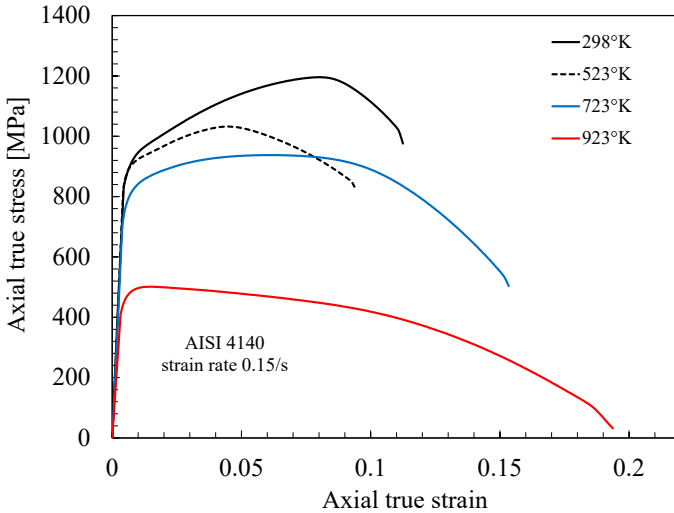


FIG. 6. Stress-strain curves at $0.15\,\mathrm{s}^{-1}$ quasi-static strain-rate.

value of nearly 0.08 (Fig. 6). At 523°K, the failure occurs at an approximate strain of 0.09 with a slope similar to that recorded at 723°K after practically a strain of 0.1, followed by a failure occurring at a 0.15 strain. At any strain-rate, a stability of deformation is generally observed at the peak temperature used (i.e., 923°K) as shown in Figs. 5 and 6. Instabilities appear in the cases of low ($T/T_f < 0.3$) and semi-elevated ($0.3 \leq T/T_f \leq 0.5$) temperatures. It is observed that variations in stress-strain curves' shape are obvious for these employed temperatures of 250°C and 450°C as also mentioned in [34]. A softening

phenomenon becomes then dominant with a negative slope of the stress-strain relationship. Changes in the deformation mechanism of the plastic provoked this softening. Dynamic recrystallization influenced the observed dislocation mobility. The alloying elements, acting as obstacles, have a slight field of stress that may lead to dislocation climb. It could also be controlled by the dynamic strain aging phenomenon which generally appears at temperatures lying in the 20–400°C range [32]. Plastic deformation can be used to enhance the nitrides and carbides formation in solid solution; however, this is sensitive to the deformation temperature employed [34]. Due to technical difficulties in grasping such mechanisms, very few works have been undertaken. At elevated temperatures, $T = 923$°K, $(T/T_f > 0.5)$, as also discussed above (Fig. 1) the four phases are driven by the competing forces of work softening and hardening (due to DRV, DRX, and variation of the grain size during deformation) and are controlled by changes in the microstructure, regardless of the quasi static strain-rate used.
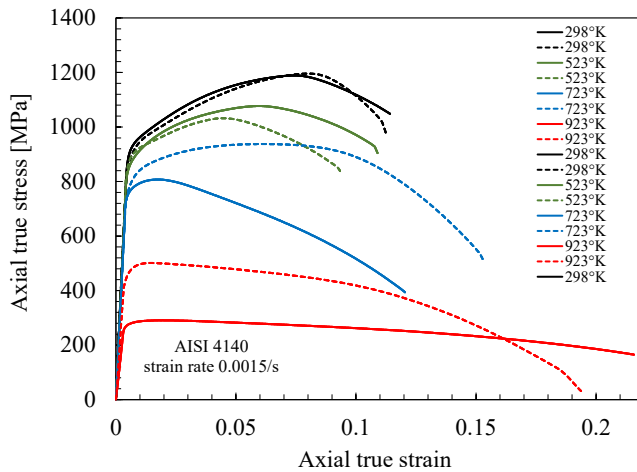


Fig. 7.  Stress-strain curves demonstrating the combined effect of strain rates and elevated temperatures on the mechanical behavior of 42CrMo.

Figure 7 illustrates the combined test results from which the conclusion that applied strain-rate affects the material response at any applied temperature can be deduced. Note that at 523°K, the behavior of the alloy at a $0.15\,\text{s}^{-1}$ strain-rate compared to that of $0.0015\,\text{s}^{-1}$ was different, and a lower ultimate tensile strength, work-hardening, and ductility were observed (Fig. 7). This requires further investigation and may be attributed to the microstructure instability of this alloy during plastic deformation. In addition to this observation, a prominent softening regime was detected at higher temperatures through the stress-strain curves; subgrain structure coarsening might be the cause of this, as discussed in [35–37]. The combination of temperature and strain-rate might be altered

during the deformation of the local dislocation mechanism prompted by DRV, DRX, grain size, etc. This also requires further investigation to fully comprehend such behavior under these thermomechanical cases.

## 2.4. Young modulus and strength

Strain-rate, temperature, and temperature/strain-rate affect 42CrMo steel's Young modulus, as demonstrated in Fig. 8. To determine the Young modulus and accurately measure the elastic and plastic strains, the neck cross-section of the specimens was fitted with strain gauges at room temperature. Afterward, all tests were conducted up to failure without the installation of strain gauges at higher temperatures (523°K, 723°K, and 932°K) and strain-rates ($0.0015 \, \text{s}^{-1}$ and $0.15 \, \text{s}^{-1}$) since the elastic modulus had already been determined. Instead, a strain correction procedure was applied to the experimental results to define the different Young moduli values and identify any differences at varying temperatures and strain rates. Accordingly, the results indicated that Young moduli do not vary significantly when the temperatures lie in the 298°K to 723°K range, irrespective of strain-rate (less than 13% variation). The Young moduli at both strain-rates considerably decrease at the highest temperature (923°K) in contrast. This disparity may be attributed to the viscous effect of 42CrMo steel on its elastic behavior (i.e. viscoelastic behavior). At 932°K, the Young modulus is 82.7 GPa and 128.6 GPa at $0.0015 \, \text{s}^{-1}$ and $0.15 \, \text{s}^{-1}$ strain-rates, respectively, which corresponds to a reduction of 58.7% and 35.7%. It should be mentioned here that accurate measurements of the elastic properties at higher tempera-
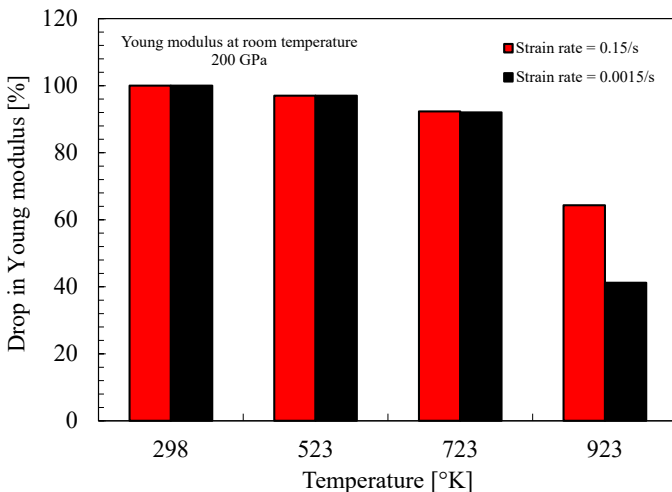


FIG. 8. Young modulus degradation versus temperatures at $0.0015 \, \text{s}^{-1}$ and $0.15 \, \text{s}^{-1}$ strain-rates.

tures require careful attention. LINDGREN and BACK [38] developed a theoretical model for steel alloys to predict the elastic properties such as shear modulus, Poison's ratio, and Bulk modulus that accounts for the temperature dependency. They also showed a strain-rate dependency of these elastic properties which support the above-mentioned variations in the elastic modulus.
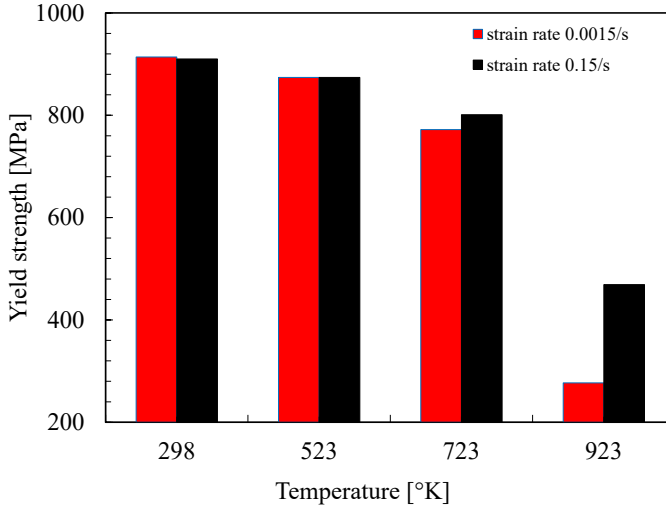


FIG. 9. Yield strength evolution versus temperatures at $0.0015\,\mathrm{s}^{-1}$ and $0.15\,\mathrm{s}^{-1}$ strain-rates.

Similarly, the dependence of yield strength on the temperature, strain-rate, and temperature/strain-rate combination were assessed. The yield stress was examined at 0.2% strain offset. The general decreasing trend in the yield strength at increasing temperatures is seen in Fig. 9. From 298°K (room temperature) up to 723°K, the yield strength decreased by no more than 17% at both strain-rates. However, at 923°K, significant reductions of 70% ($\sigma_y = 277\,\mathrm{MPa}$) and 49% ($\sigma_y = 470\,\mathrm{MPa}$) were observed at $0.0015\,\mathrm{s}^{-1}$ and $0.15\,\mathrm{s}^{-1}$ strain-rates, respectively. Accordingly, 42CrMo shows more sensitivity at temperatures much higher than room temperature for an applied strain-rate.

### 2.5. Work-hardening modulus

Aside from the yield strength, the work-hardening modulus was used to characterize work-hardening behavior. The stress-strain curve's slope can be utilized to obtain the work hardening modulus, which varies with time during transformation. The effect of the three factors: (i) temperature, (ii) strain-rate, and (iii) temperature/strain-rate combination on the work-hardening modulus was studied. Figures 10 and 11 illustrate the variations of the hardening moduli with the strain for $0.0015\,\mathrm{s}^{-1}$ and $0.15\,\mathrm{s}^{-1}$ strain-rates, respectively, validating the
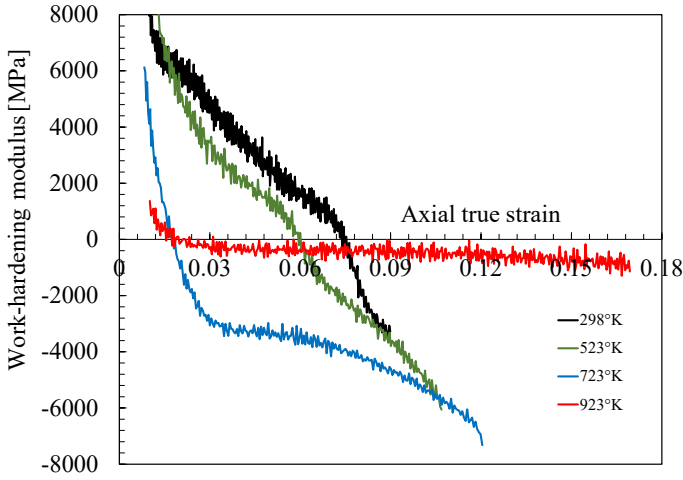
Fig. 10. Hardening modulus evolution against strain at varying temperatures and a $0.0015\,\mathrm{s}^{-1}$ strain-rate.
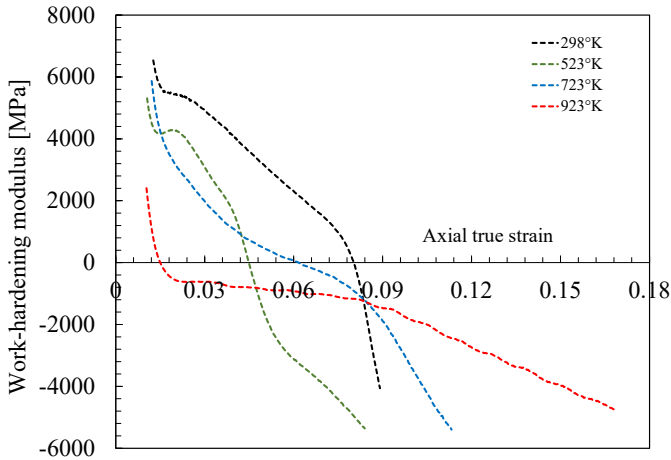


Fig. 11. Hardening modulus evolution against strain at different temperatures and a $0.15\,\mathrm{s}^{-1}$ strain-rate.

significance of the three aforementioned parameters on this modulus. A positive hardening evolution phase and a negative hardening evolution phase were taken into consideration, irrespective of the temperature and the strain-rate, and the zero-hardening modulus corresponded to the ultimate tensile strength (or the end of the phase (ii)). Generally, at lower temperatures (i.e., 298°K and 523°K) and lower strain-rate, higher hardening is observed. At $0.0015\,\mathrm{s}^{-1}$, the evolution of positive strain-hardening moduli was noted (Fig. 10). The values of the zero-hardening moduli were deduced at 0.074 and 0.06 strains for 298°K and 523°K,

respectively. At higher temperatures (i.e. 723°K and 923°K), in contrast, less hardening is observed. The induced zero-hardening moduli were deduced at approximately 0.018 strains for both temperatures. However, for higher temperatures, the negative moduli behave differently. At 723°K, stress-softening occurs relatively gradually until failure (Figs. 5 and 10). On the other hand, a negative hardening evolution with a low rate of change occurs at 923°K, as shown in Fig. 10. This is fully controlled by these local mechanisms mentioned above.

At the same temperatures but at a higher strain-rate ($0.15\,\mathrm{s}^{-1}$), higher modulus evolutions are noted (Fig. 11). Indeed, at 723°K, the modulus does not develop as anticipated because of the deformation mechanism of the alloy changes under this thermomechanical combination due to the instabilities of microstructures. One of these instabilities is the dynamic strain aging. Because of phase (iii) and phase (iv) effect, a negative modulus is recorded at this strain-rate across a long scope of plastic strain at 923°K, the highest temperature.
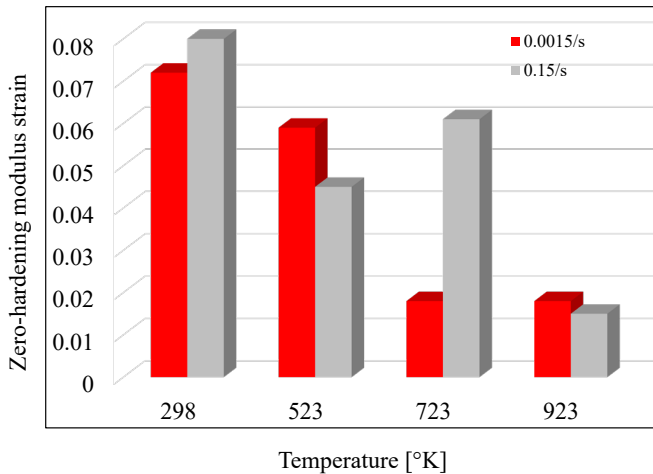


FIG. 12. Zero-hardening modulus strain evolution versus temperature under $0.0015\,\mathrm{s}^{-1}$ and $0.15\,\mathrm{s}^{-1}$ strain-rates.

Figure 12 conveys the strains that correspond to the zero-hardening moduli, for the applied temperature and strain-rate. From the observations made thus far, the behavior of 42CrMo alloy deviates from the general trend at 723°K compared to other temperatures, which requires further examination at the local level.

## 2.6. Dynamic strain aging

Irregularities in flow stress curves of low-carbon steels and aluminum alloys often describe dynamic strain aging (DSA). The different features of the DSA depend on the microstructure of the steel. This impinges on the nucleation dy-

namics and deformation bands propagation as shown in [39, 40]. DSA becomes more pronounced at specific strains lying in a particular regime of strain-rates and temperatures (0.2–0.5 Tm) [41]. Primarily, the DSA mechanism is attributed due to the dynamic interaction between mobile dislocations and diffusing solute interstitials such as C and N [42–44]. Once the temperature increases, this leads to improving the diffusivity of solute atoms and the mobility of dislocations. Therefore, one can expect that the DSA intensity arises via a specific temperature and strain-rate combination.

The DSA behavior was determined at three strain levels of 0.002, 0.05, and 0.09 for four different temperatures, and two strain-rates of $0.0015\,\mathrm{s}^{-1}$ and $0.15\,\mathrm{s}^{-1}$ were plotted, respectively in Figs. 13 and 14. The three strain levels were chosen to cover a uniform deformation range. A degradation curve concaved upward typically illustrates the relationship between flow-stress degradation and increasing temperatures. The peaks/jumps in the flow stress can clearly be noted at different strain rates and temperature combinations, which correspond to active DSA. At $\dot{\varepsilon} = 0.0015\,\mathrm{s}^{-1}$. The DSA performance is noticeably observed at 523°K and 723°K at strain levels up to 0.05 (Fig. 13). However, the stress jump was only observed at 723°K for strain level of 0.09. Similar observations were made at $\dot{\varepsilon} = 0.15\,\mathrm{s}^{-1}$, where DSA was active within the same range of temperatures and was also observed at 723°K for strain level of 0.09 (Fig. 14). It is obvious that, for a given strain-rate, temperature is not the only factor that affects the DSA, but also the level of plastic deformation. The effect of DSA on yield strength is still somewhat ambiguous; however, the effect is improved with increasing levels of plastic deformation. One possible explanation is: increasing
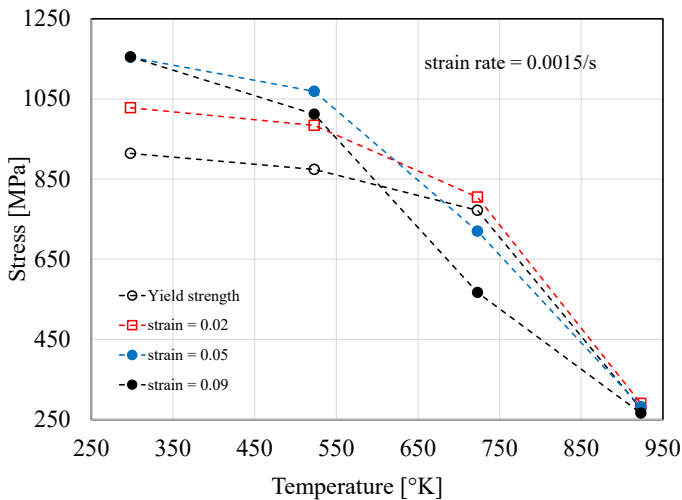


Fig. 13. Stress variation versus temperatures for $0.0015\,\mathrm{s}^{-1}$ strain-rate at various strain levels.
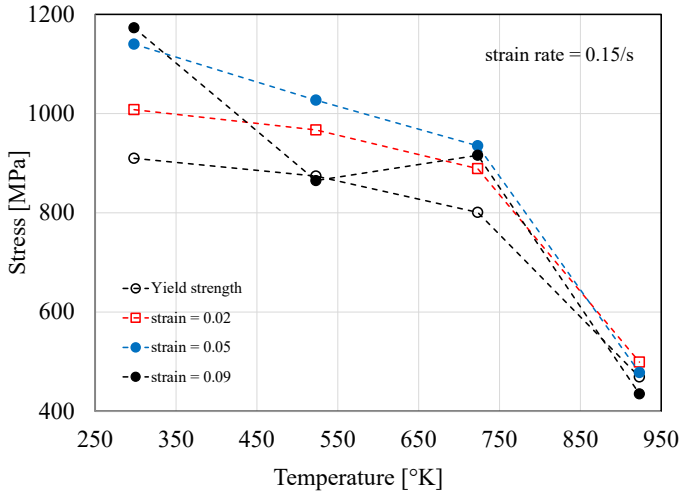
Fig. 14. Stress variation versus temperatures for $0.15\,\mathrm{s}^{-1}$ strain-rate at various strain levels.

the plastic strain can improve the dynamic interchange between mobile dislocations and solute atoms due to the appearance of the dislocation mobility [45–47].

## 2.7. Scanning Electron Microscope (SEM)

The 42CrMo steel microstructure at failure should be studied to gain a deeper understanding of the thermomechanical performance of metals. The different loading rate/temperature combinations induce void nucleation, growth and coalescence which require further investigation. These internal damages are concentrated close to the fracture surface at which the highest localization of plastic strains and the related stresses is observed. Scanning electron microscopy (SEM) is one of the well-known tools that are able to measure the damaged areas (area fraction of voids), providing qualitative and quantitative analysis. Figure 15 shows samples of 42CrMo micrographs which examine the surface of the tensile specimens during fracture under different temperatures and at suitable magnifications.

Defect-area fractions observed at room temperature were lower than those observed for fracture surfaces exposed to higher temperatures (Fig. 15). At increasing temperatures, for a given strain-rate, more damage evidently occurs in the specimens (i.e., void area fraction increases). The highest damage area is noted at higher temperatures as presented in Fig. 15, which also shows a higher fraction of void area at the more elevated temperatures (i.e., greater than the ambient valueas indicated by the darker areas on the images). This observation can be attributed to the high strain-sensitivity of 42CrMo steel at increasing temperatures (viscoplastic damaged response). Moreover, for greater strain-rates at the
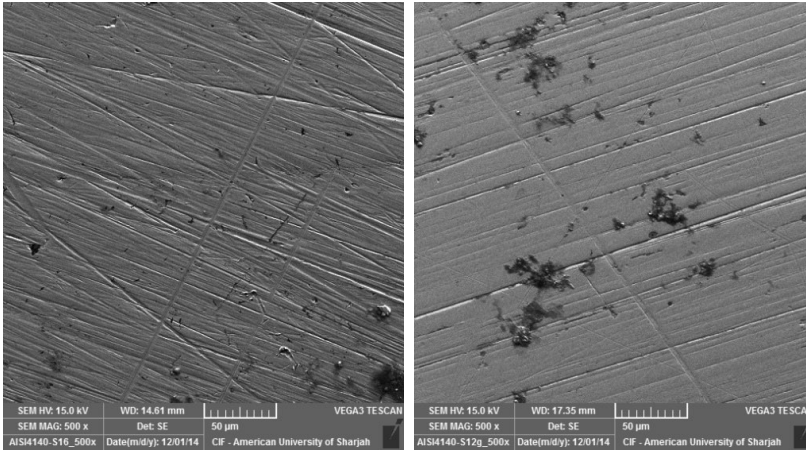
Fig. 15. Sample of SEM images of fractured 42CrMo specimens at a $0.0015\,\mathrm{s}^{-1}$ strain-rate and room and high temperatures.

same temperatures, this observation is less pronounced. An explanation for this behavior could be because the voids do not expand as much due to the shorter time span. Beyond this, it should be highlighted that 42CrMo's sensitivity to the strain-rate increases with increasingly elevated temperature; therefore, the overall accumulated strain then is considered a central part in the determination of the fraction of void area.

## 2.8. Dynamic behavior – drop hammer tests

The dynamic response of 24CrMo steel can be influenced by two major elements: (i) metals' flow-stress and sensitivity to the strain-rate applied and (ii) the inertia forces' effect on the deformation mode of the structure. Specimens, as such, show consistent deformation when exposed to quasi-static loading and a non-uniform deformation at dynamic conditions, because of the shock-wave effect [48]. When the impact velocities used are comparatively low (below $30\,\mathrm{m/s}$) and the mass ratio of the striker/specimen is above 14 [49–51], the effect of inertia forces is negligible. Because of the applicability of these two values to the dynamic assessments performed in the work presented in this paper, the specimens were assumed to deform uniformly. A Chebyshev filter was used to smooth the force-displacement curves measured to reduce the shock effect. The true strain-true stress curves for 42CrMo were plotted and are shown in Fig. 16.

It is relatively complex to identify the yield strength and flow stress for this alloy through this test setup. Generally, it was observed that after impact, the stresses instantly increase until the ultimate dynamic stress is attained. After, the stresses start to decrease. The variations noted in these three scenarios
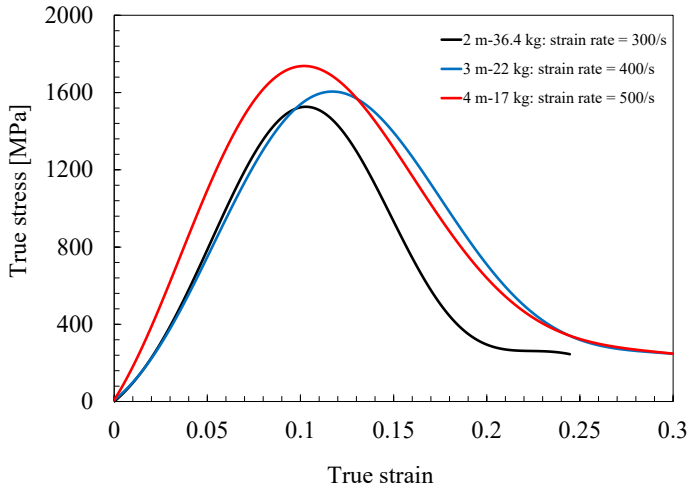
FIG. 16. Dynamic true stress-true strain curves for drop mass bench tests under different strain-rates.

pertains to the ultimate stresses which increase with increasing strain-rates (as three different hammer masses and drop-heights were used).

The true stress – true strain curve of the cylindrical samples tested with a 36.4 kg mass dropped from a 2 m height is illustrated in Fig. 16. These test parameters resulted in the lowest stress-strain response as they correspond to the lowest applied strain-rate of $300\,\mathrm{s}^{-1}$. Conversely, the highest stress level was observed from the highest drop-height of 4 m, which corresponds to the highest applied strain-rate of $500\,\mathrm{s}^{-1}$. Figure 17 illustrates the ultimate stress
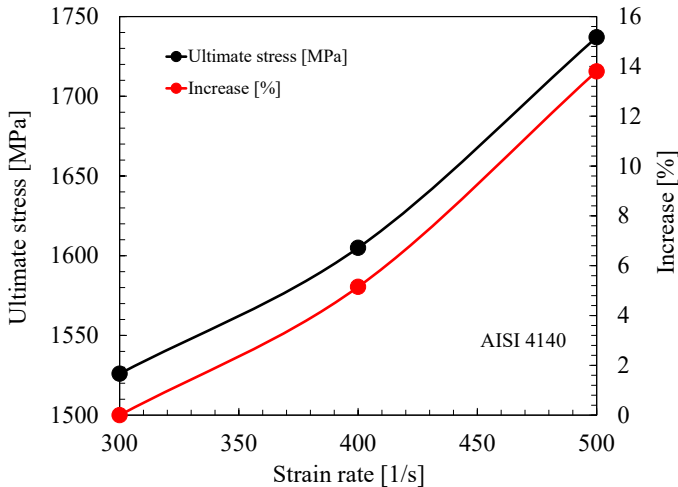


FIG. 17. Evolution of ultimate stress and its percentage increase versus dynamic strain-rate.

development with respect to the dynamic strain-rate. As portrayed by the figure, the ultimate stress increased by up to 14% at a $500\,\mathrm{s}^{-1}$ strain-rate.

## 3. Constitutive modeling

Steel flow stress can be described by incorporating an evolution mechanism for the damage into a precise plasticity model to observe the high strength alloy's stress-strain behavior. Note that the damage-induced anisotropic behavior is due to the microcrack distributions and the way they develop within metals. Many authors have proposed various damage models that consider anisotropic and/or isotropic expressions when calculating the damage variable [13–15, 52]. While the nature of the damage is anisotropic, assuming it as isotropic still yields probable results in many cases. A damage model based on energy was proposed by Abed *et al.* [13] using continuum damage mechanics principles to predict the nature by which defects in steel alloys evolve. In this model, the evolution equation of the damage variable, $\phi$, is directly related to the increase in the material dissipated energy, $U_p$, as shown in Eq. (3.1):

$$(3.1) \qquad \phi = \phi_f \left( \frac{U_p}{U_p^T} \right)^{\alpha},$$

where SEM images are used to measure the damage at fracture, $\phi_f$, $U_p^T$ represents total dissipated energy, and $\alpha$ is a constant that defines the damage evolution trend across the process of deformation, typically taken as 2.0 for most steel alloys [13].

Many flow stress models have been constructed to explain the nonlinear behavior of materials exposed to elevated strain-rates and temperatures. The models developed describe the variations in the mechanical properties and can be of various types, including semi-empirical, empirical or based on the material accumulated deformation. In this work, the Voyiadjis–Abed model (VA), which is physically-based, was used in describing the steel alloy's flow stress.

In 2005, the VA model was introduced to predict the flow stress of FCC, BCC and HCP pure metals, with a focus on the microstructure [53, 54]. Dislocations interactions mechanisms and thermal activation were both considered when deriving the model. The model's framework relates the constitutive equation's coefficients to the microstructure so that it considers the coupling dependence of strain-rate and temperature on deformation. Recently, various microstructures of pure metals' failure mechanisms have been combined in the VA model to accurately predict the flow stress for ferrite and austenite steel alloys [55, 56] as well as titanium alloys. The former is utilized in this work for the simulation of the thermomechanical response of 42CrMo steel in the applied temperature and strain-rate range.

The 42CrMo alloy's observed experimental results shows that initial yielding mainly controls the thermal mechanism whereas the strain hardening has a lower dependence. The flow stress definition proposed by the VA model for this alloy is decomposed additively into 2 parts: thermal and athermal; the relationship between these parts and the hardening and yielding can be represented by:

$$(3.2) \qquad \sigma = \overbrace{c_1 + c_2\varepsilon_p^{c3}}^{\text{athermal stress}} + \overbrace{c_4(1 - (c_5T - c_6T\ln\dot{\varepsilon}_p)^{1/q_1})^{1/q_2}}^{\text{thermal stress}},$$

where the exponents $q_1$ and $q_2$ are constants that define the short-range barrier's shape, considered as 1.5 and 0.5 in this study, respectively. The variables $c_1$ to $c_6$ are material constants and are mathematically correlated to the microstructural physical quantities as shown below:

$$(3.3) \qquad \mathbf{c_1} \propto \mu\sqrt{\frac{b}{D_g}}, \quad \mathbf{c_2} \propto \mu b, \quad \mathbf{c_4} \propto \mu_0\frac{b^2}{A_0}, \quad \mathbf{c_5} \propto b\nu_0\rho, \quad \mathbf{c_6} \propto \frac{K}{G_0},$$

where $K$ is Boltzmann's constant, $G_0$ represents the reference Gibbs energy at absolute temperature $T$ in Kelvin, $\mu$ is the shear modulus, $\mu_0$ is the sheer modulus value at absolute temperature, $D_g$ is the grain diameter, $A_0$ is the dislocation activation area, $\rho$ is the dislocation density, $b$ is the Burgers vector magnitude, and $\nu_0 = d/t_w$ is the reference dislocation velocity with $d$ representing the average distance moved by the dislocation between barriers and $t_w$ representing the time taken by a dislocation while waiting at a barrier.

Table 2 summarizes all the experimentally derived VA model constants for 42CrMo steel alloy. The utilization of these material constants plays an important role in the prediction of flow stress via finite element simulation, as is discussed next. However, it is important to note that revisions may be required to determine the model constants' accuracy by expanding the scope of strain-rates used. In addition, the role of solute/dislocation interaction was not considered in this work; hence, the model prediction may not be accurate at strain, strain-rates, and temperatures lying in the range whereby dynamic and static strain aging are prominent.

**Table 2. Parameters of the VA model for 42CrMo steel alloy.**

| Material | $C_1$ [MPa] | $C_2$ [MPa] | $C_3$ | $C_4$ [MPa] | $C_5$ | $C_6$ |
|---|---|---|---|---|---|---|
| 42CrMo | 150 | 770 | 0.20 | 1850 | 0.00091 | $2.1 \times 10^{-5}$ |

## 4. Finite element simulation

The finite element (FE) simulation discussed in this section was utilized mainly to validate the VA model and to verify its applicability in simulating the

drop hammer test performed experimentally. The commercial software ABAQUS was used to conduct the FE modeling [57]. Two FE models were designed and developed for achieving the aforementioned purpose, as is discussed next.

### 4.1. VA model validation

Before simulating large-scale cases, the VA model FE implementation was validated using a simple uniaxial tensile test of one element. The dimensions employed in this analysis is $20\,\text{mm} \times 20\,\text{mm}$. Due to the symmetry present, modeling a quarter of the problem is adequate. To guarantee that strain-rate values are equal to $0.0015\,\text{s}^{-1}$, $0.015\,\text{s}^{-1}$, and $0.15\,\text{s}^{-1}$, loading profiles, expressed with respect to applied displacement, were employed at $1.5 \times 10^{-5}\,\text{m/s}$, $1.5 \times 10^{-4}\,\text{m/s}$, and $1.5 \times 10^{-3}\,\text{m/s}$ velocities, respectively.

After developing the model, the uniaxial stress-strain results were obtained by incorporating the FE analysis into the model. The predicted stress-strain results obtained from the VA model and the 42CrMo experiments were compared; these comparisons are shown in Fig. 18. The VA model was able to reasonably predict the stresses trends and values at room temperature for the two quasi-static loading rates. Thus, the results of the verification analysis were deemed satisfactory and the model was considered adequate in simulating the material behavior under room temperature.
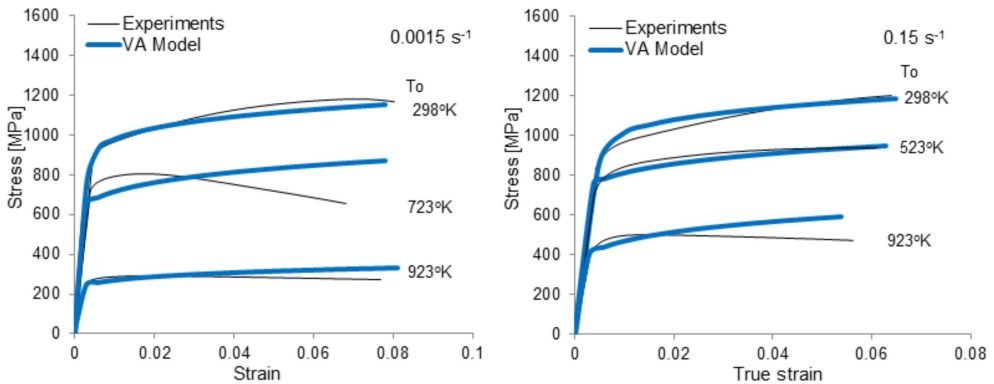


Fig. 18. FE prediction of stress-strain curves for 42CrMo steel at $0.0015\,\text{s}^{-1}$ and $0.15\,\text{s}^{-1}$ strain-rates.

### 4.2. Drop hammer test simulation

A simulation of the drop hammer tests conducted during the experiments was done by utilizing a test arrangement identical to the one previously discussed with respect to the drop heights, specimen dimensions, and hammer weights. An axisymmetric FE formulation was used when modelling the specimen due to
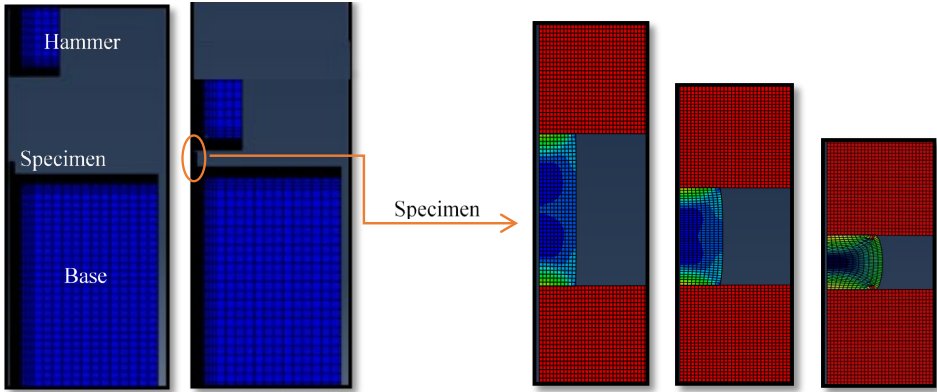
Fig. 19. Drop hammer test's FE deformation process and mesh configurations for a drop hammer test.

it being shaped as a cylinder. The drop hammer test FE model comprised of rigid and solid portions; the base and the hammer were considered as rigid while a deformable solid model was used for the specimens. Axisymmetric elements were used to mesh every part; however, the configurations of the mesh differed for each portion, as displayed in Fig. 19. Small elements (i.e. fine meshing) were used to mesh the specimen in a uniform fashion. The hammer and the ground parts, on the other hand, utilized two distinct mesh controls while meshing; fine mesh configurations, similar to the specimen's mesh control, were used to model the areas directly contacting the specimen while a coarse mesh configuration was assigned to the areas that were not close to contacting the specimen.

It is important to accurately mimic the drop hammer tests loading conditions; therefore, the hammer free fall simulation was allocated a gravitational load with
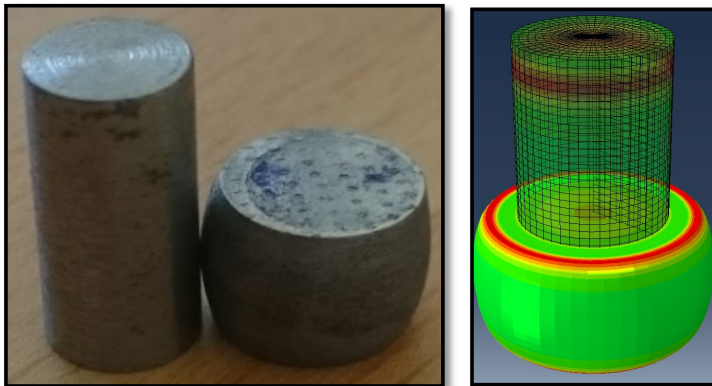


Fig. 20. A comparisons experimental and FE simulation results for the specimen's shape of deformation.

a $9.81\,\mathrm{m/s^2}$ acceleration value. A self-contact interaction mechanism is adopted between the specimen surfaces of the specimens at both the hammer and base ends. Since these types of tests results in intermediate deformation strain-rates, the analysis considered adiabatic deformation by assuming that the dissipation of the generated heat (due to the plastic work) to its surroundings is 50%. An example of the process by which the drop hammer deforms at varying time increments is displayed in Fig. 20.

To verify the drop hammer test FE simulation, the computational and experimental results were compared with special regards to the shape of deformation and the specimen failure. The specimen deformed configuration and final dimensions were acceptably comparable to their experimental counterparts. Figure 20 illustrates an example of one of the comparisons performed.

## 5. Summary and conclusions

It is necessary to investigate 42CrMo high strength steel thermomechanical behavior and response for various purposes, including design and construction. In this study, 42CrMo steel behavior is studied for a wide scope of temperatures and strain-rates. The results showed three deformation regimes due especially to the applied temperature ranges (low, semi-elevated, and elevated temperatures). To inspect the thermomechanical behavior of this alloy, multiple uniaxial tensile tests were performed at varying quasi-static strain-rates ($0.0015\,\mathrm{s^{-1}}$, $0.015\,\mathrm{s^{-1}}$, and $0.15\,\mathrm{s^{-1}}$) and temperatures (298°K, 523°K, 723°K and 923°K). Additionally, a drop mass bench was used to conduct dynamic tests at room temperature at $300\,\mathrm{s^{-1}}$, $400\,\mathrm{s^{-1}}$, and $500\,\mathrm{s^{-1}}$ compressive dynamic strain-rates. To ensure iso-energy conditions are maintained during the characterization of the steel dynamic behavior, three different hammer masses were released from three distinct heights to test multiple cylindrically shaped samples.

During plastic deformation that is being affected by the temperature/strain-rate combination, key features like work-hardening and thermally activated softening are driving forces modifying the alloy microstructure. They have a substantial role in the determination of the alloy's mechanical properties. Results showed that 42CrMo steel quasi-static responses at room temperature were almost insignificantly dependent on the quasi-static strain-rate. Sensitivity to strain-rate increases in effectiveness with increasing temperatures at which hardening-softening competition occurs. Therefore, the impact of strain-rate, temperature, and their coupling on the Young's modulus, yield strength, work-hardening, and its modulus was investigated.

On the other hand, certain temperature/strain-rate combinations led to the occurrence of dynamic strain aging (DSA); the DSA increased with increasing strain. Characterization of DSA is mostly done by examining the abrupt jumps

in thermal stress as it varies at different temperatures. At 523°K and 723°K, this DSA phenomenon was noticeable in 42CrMo steel for both quasi-static strain-rates.

Identification of the material constants present in the constitutive, physically-based VA model was established by utilizing the stress-strain responses of 42CrMo. The parameters of the VA model that were extracted from the experimental data displayed good results, particularly at temperatures and strain-rate combinations where the DSA was not effective. The experimental results were then reproduced by implementing the VA model into ABAQUS, an FE software, and the dynamic hammer tests were simulated. It is important to note that the objective of this work is to target applications that give rather intermediate strain-rates than high rates. Thus, the drop hammer represents an appropriate choice from the point of view of the strain rate. The numerical analysis was mainly utilized to develop a robust FE model capable of expanding and simulating a variety of structural problems involving the usage of 42CrMo in large-scale practical applications exposed to various loading conditions.

Scanning electron microscopy (SEM) was employed in understanding the material microstructure and measuring the internal voids and micro-cracks at fracture for each test condition. The impact temperature and strain-rate exert on micro-cracks and/or voids within these steel at fracture were analyzed. For this steel, the damage accumulation was significantly dependent on the strain-rate, temperature, and plastic straining quantity at fracture.

## Acknowledgements

## References

1. A. Kundu, D.P. Field, P.C. Chakraborti, *Effect of strain and strain-rate on the development of deformation heterogeneity during tensile deformation of a solution annealed 304 LN austenitic stainless steel: an EBSD study*, Materials Science and Engineering: A, **773**, 138854, 2020.

2. B. Jia, A. Rusinek, R. Pesci, S. Bahi, R. Bernier, *Thermo-viscoplastic behavior of 304 austenitic stainless steel at various strain-rates and temperatures: testing, modeling and validation*, International Journal of Mechanical Sciences, **170**, 105356, 2020.

3. J. Gordon, J. Hochhalter, C. Haden, D.G. Harlow, *Enhancement in fatigue performance of metastable austenitic stainless steel through directed energy deposition additive manufacturing*, Materials & Design, **168**, 107630, 2019.

4. M. Güden, S. Enser, M. Bayhan, A. Taşdemirci, H. Yavaş, *The strain-rate sensitive flow stresses and constitutive equations of a selective-laser-melt and an annealed-rolled 316L stainless steel: a comparative study*, Materials Science and Engineering: A, **838**, 142743, 2022.

5. T.S. Kumar, A. Nagesha, K. Mariappan, M.K. Dash, *Deformation and failure behaviour of 316 LN austenitic stainless-steel weld joint under thermomechanical low cycle fatigue in as-welded and thermally aged conditions*, International Journal of Fatigue, **149**, 106269.

6. F. Abed, A. Abdul-Latif, A. Yehia, *Experimental study on the mechanical behavior of EN08 steel at different temperatures and strain-rates*, Metals, **9**, 736–745, 2018.

7. F. Abed, M. Saffarini, A. Abdul-Latif, G.Z. Voyiadjis, *Flow stress and damage behavior of C45 Steel over a range of temperatures and loading rates*, ASME-Journal of Engineering Materials and Technology, **139**, 02101–02102, 2017.

8. H.F. Abed, A.K. Al-Tamimi, R.M. Al-Himairee, *Characterization and modeling of ductile damage in structural steel at low and intermediate strain-rates*, Journal of Engineering Mechanics, **138**, 9, 1186–1194, 2012.

9. M. Varga, S. Leroch, T. Gross, H. Rojacz, S.J. Eder, M. Grillenberger, M.R. Ripoll, *Scratching aluminium alloys–modelling and experimental assessment of damage as function of the strain-rate*, Wear, **476**, 203670, 2021.

10. F. Abed, F. Makarem, *Comparisons of constitutive models for steel over a wide range of temperatures and strain-rates*, Journal of Engineering Materials and Technology, **134**, 2, 021001, 2012.

11. A. Abdul-Latif, K. Saanouni, *Damaged an elastic behavior of FCC polycrystalline metals with micromechanical approach*, International Journal of Damage Mechanics, **3**, 237, 1994.

12. M. Chadli, A. Abdul-Latif, *Meso-damage evolution in polycrystals*, ASME, Engineering Materials and Technology, **127**, 214–221, 2005.

13. R.A. Lebensohn, A.D. Rollett, *Spectral methods for full-field micromechanical modelling of polycrystalline materials*, Computational Materials Science, **173**, 109336, 2020.

14. F.H. Abed, S.I. Ranganathan, M.A. Serry, *Constitutive modeling of nitrogen-alloyed austenitic stainless steel at low and high strain-rates and temperatures*, Mechanics of Materials, **77**, 142–157, 2014.

15. F.H. Abed, *Constitutive modeling of the mechanical behavior of high strength ferritic steels for static and dynamic applications*, Mechanics of Time-Dependent Materials, **14**, 4, 329–345, 2010.

16. G. Voyiadjis, F. Abed, *Transient localizations in metals using microstructure-based yield surfaces*, Modelling and Simulation in Materials Science and Engineering, **15**, 1, S832006, 2006.

17. F. Abed, C. ElSayegh, A. Abdul-Latif, *Thermomechanical Description of AISI4140 Steel at Elevated Temperatures*, Proceedings of the TMS Middle East–Mediterranean Materials Congress on Energy and Infrastructure Systems (MEMA 2015), pp. 491–499, Springer, 2015.

18. J. STEWART, B. ALEXANDROV, *Quantification of the hardness response in the heat-affected zone of low alloy steels subjected to temper bead welding*, Journal of Manufacturing Processes, **66**, 325–340, 2021.

19. B. HAN, R. ZHU, C. FENG, W. LI, G. WEI, Z. WANG, Q. LI, $CO_2$ *effective conversion in Fe-C-Al-Si molten steel under vacuum conditions*, Vacuum, **179**, 109520, 2020.

20. A. MEYSAMI, R. GHASEMZADEH, S. SEYEDEIN, M. ABOUTALEBI, *An investigation on the microstructure and mechanical properties of direct-quenched and tempered AISI 4140 steel*, Materials & Design, **31**, 3, 1570–1575, 2010.

21. J. SCHWALM, M. GERSTENMEYER, F. ZANGER, V. SCHULZE, *Complementary machining: effect of tool types on tool wear and surface integrity of AISI 4140*, Procedia CIRP, **87**, 89–94, 2020.

22. C. WANG, Q. GUO, M. SHAO, H. ZHANG, F. WANG, B. SONG, H. LI, *Microstructure and corrosion behavior of linear friction welded TA15 and TC17 dissimilar joint*, Materials Characterization, 111871, 2022.

23. C. JIANG, X. ZHANG, D. WANG, L. ZHANG, X. CHENG, *Phosphate conversion coatings on 35CrMnSi steels subjected to different heat treatments*, Electrochemistry Communications, **110**, 106636, 2020.

24. D. KAISER, J. DAMON, F. MÜHL, B. DE GRAAFF, D. KIEFER, S. DIETRICH, V. SCHULZE, *Experimental investigation and finite-element modeling of the short-time induction quench-and-temper process of AISI 4140*, Journal of Materials Processing Technology, **279**, 116485, 2020.

25. U. THAMMA, P. JANTASORN, *Effects of shear deformation via torsion on tensile strain-hardening behavior of SCM415 low-alloy steel*, Materials Today: Proceedings, 2021.

26. H. ZHU, H. OU, *Constitutive modelling of hot deformation behaviour of metallic materials*, Materials Science and Engineering: A, **832**, 142473, 2022.

27. L. GUO, F. WANG, P. ZHEN, X. LI, M. ZHAN, *A novel unified model predicting flow stress and grain size evolutions during hot working of non-uniform as-cast 42CrMo billets*, Chinese Journal of Aeronautics, **32**, 2, 531–545, 2019.

28. Y. WU, Y. JIA, S. ZHANG, Y. LIU, H. XIONG, G. CHEN, *Flow softening and dynamic recrystallization behavior of a Mg-Gd-Y-Nd-Zr alloy under elevated temperature compressions*, Journal of Magnesium and Alloys, 2021, doi: 10.1016/j.jma.2021.11.009.

29. K. SURESH, K.P. RAO, Y.V.R.K. PRASAD, N. HORT, K.U. KAINER, *Study of hot forging behavior of as-cast Mg–3Al–1Zn–2Ca alloy towards optimization of its hot workability*, Materials & Design, **57**, 697–704, 2014.

30. A.M. PHILIP, K. CHAKRABORTY, *Some studies on the machining behaviour of 316L austenitic stainless steel*, Materials Today: Proceedings, 2022.

31. J. ZHAO, Z. LIU, B. WANG, J. HU, Y. WAN, *Tool coating effects on cutting temperature during metal cutting processes: Comprehensive review and future research directions*, Mechanical Systems and Signal Processing, **150**, 107302, 2021.

32. M.S. CHEN, Y.C. LIN, X.S. MA, *The kinetics of dynamic recrystallization of 42CrMo steel*, Materials Science and Engineering: A, **556**, 260–266, 2012.

33. N. RANC, D. WAGNER, *Some aspects of Portevin–Le Chatelier plastic instabilities investigated by infrared pyrometry*, Materials Science and Engineering: A, **394**, 87–95, 2005.

34. P.F. Giroux, F. Dalle, M. Sauzay, J. Malaplate, B. Fournier, A.F. Gourgues-Lorenzon, *Mechanical and microstructural stability of P92 steel under uniaxial tension at high temperature*, Materials Science and Engineering: A, **527**, 3984–3993, 2010.

35. J. Eisenträger, K. Naumenko, H. Altenbach, E. Gariboldi, *Analysis of temperature and strain-rate dependencies of softening regime for tempered martensitic steel*, The Journal of Strain Analysis for Engineering Design, **52**, 226–238, 2017.

36. S. Alsagabi, T. Shrestha, I. Charit, *High temperature tensile deformation behavior of Grade 92 steel*, Journal of Nuclear Materials, **453**, 151–157, 2014.

37. D. Yuzbekova, A. Mogucheva, D. Zhemchuzhnikova, T. Lebedkina, M. Lebyodkin, R. Kaibyshev, *Effect of microstructure on continuous propagation of the Portevin–Le Chatelier deformation bands*, International Journal of Plasticity, **96**, 210–226, 2017.

38. L.-E. Lindgren, J.G. Back, *Elastic properties of ferrite and austenite in low alloy steels versus temperature and alloying*, Materialia, **5**, 3, 100193, 2019.

39. D. Zhemchuzhnikova, M. Lebyodkin, D. Yuzbekova, T. Lebedkina, A. Mogucheva, R. Kaibyshev, *Interrelation between the Portevin Le–Chatelier effect and necking in AlMg alloys*, International Journal of Plasticity, **110**, 95–109, 2018.

40. T. Wang, J. Jonas, H. Qin, S. Yue, *Effect of dynamic strain aging on the deformation and twinning behavior of a Mg–2Zn–2Nd alloy*, Materials Science and Engineering: A, **645**, 126–135, 2015.

41. A.H. Cottrell, LXXXVI. *A note on the Portevin–Le Chatelier effect*, Materials Science and Engineering, **744**, 355, 829–832, 1953.

42. S.-J. Lee, J. Kim, S.N. Kane, B.C.D. Cooman, *On the origin of dynamic strain aging in twinning-induced plasticity steels*, Acta Materialia, **59**, 6809–6819, 2011.

43. F. Yang, H. Luo, E. Pu, S. Zhang, H. Dong, *On the characteristics of Portevin–Le Chatelier bands in cold-rolled 7Mn steel showing transformation-induced plasticity*, International Journal of Plasticity, **103**, 188–202, 2018.

44. R.C. Picu, *A mechanism for the negative strain-rate sensitivity of dilute solid solutions*, Acta Materialia, **52**, 3447–3458, 2004.

45. F. Shen, S. Münstermann, J. Lian, *An evolving plasticity model considering anisotropy, thermal softening and dynamic strain aging*, International Journal of Plasticity, doi: 10.1016/j.ijplas.2020.102747, 2020.

46. G.Z. Voyiadjis, Y. Song, A. Rusinek, *Constitutive model for metals with dynamic strain aging*, Mechanics of Materials, **129**, 353–360, doi: 10.1016/j.mechmat.2018. 12.012, 2019.

47. C.R. Calladine, R.W. English, *Strain-rate and inertia effect in the collapse of the two types of energy-absorbing structure*, International Journal of Mechanical Sciences, **26**, 11/12, 689–701, 1984.

48. R. Wang, C.Q. Ru, *An energy criterion for dynamic plastic buckling of circular cylinders under impulsive loading*, in: *Metal Forming and Impact Mechanics*, S.R. Reid [ed.], pp. 213–223, Pergamon, New York, 1985.

49. A. Abdul-Latif, R. Baleh, *Dynamic biaxial plastic buckling of circular shells*, ASME, Journal of Applied Mechanics, **75**, 3, 031013, 2008.

50. R. Baleh, A. Abdul-Latif, A. Menouer, D. Razafindramary, *New experimental investigation of non-conventional dynamic biaxial plastic buckling of square aluminum tubular structures*, International Journal of Impact Engineering, **122**, 333–345, 2018.

51. G.Z. Voyiadjis, T. Park, *Anisotropic damage for the characterization of the onset of macro-crack initiation in metals*, International Journal of Damage Mechanics, **5**, 1, 68–92, 1996.

52. G.Z. Voyiadjis, F.H. Abed, *Microstructural based models for bcc and fcc metals with temperature and strain-rate dependency*, Mechanics of Materials, **37**, 355–378, 2005.

53. G.Z. Voyiadjis, F.H. Abed, *Effect of dislocation density evolution on the thermomechanical response of metals with different crystal structures at low and high strain-rates and temperatures*, Archives of Mechanics, **57**, 4, 299–343, 2005.

54. F.H. Abed, S.I. Ranganathan, M.A. Serry, *Constitutive modeling of nitrogen-alloyed austenitic stainless steel at low and high strain-rates and temperatures*, Mechanics of Materials, **77**, 142–157, 2014.

55. F.H. Abed, *Constitutive modeling of the mechanical behavior of high strength ferritic steels for static and dynamic applications*, Mechanics of Time-Dependent Materials, **14**, 4, 329–345, 2010.

56. A. Tabei, F. Abed, G.Z. Voyiadjis, H. Garmestani, *Constitutive modeling of Ti-6Al-4V at a wide range of temperatures and strain-rates*, European Journal of Mechanics-A/Solids, **63**, 128–135, 2017.

57. A. Smith, ABAQUS/Explicit, Simulia, 2018.